Predicting image properties in penalized-likelihood reconstructions of flat-panel CBCT

Wenying Wang, Grace J. Gang, Jeffrey H. Siewerdsen, and J. Webster Stayman[a)]
Department of Biomedical Engineering, Johns Hopkins University, Baltimore, MD 21205, USA

(Received 26 June 2018; revised 17 September 2018; accepted for publication 9 October 2018; published 20 November 2018)

Purpose: Model-based iterative reconstruction (MBIR) algorithms such as penalized-likelihood (PL) methods exhibit data-dependent and shift-variant properties. Image quality predictors have been derived to prospectively estimate local noise and spatial resolution, facilitating both system hardware design and tuning of reconstruction methods. However, current MBIR image quality predictors rely on idealized system models, ignoring physical blurring effects and noise correlations found in real systems. In this work, we develop and validate a new set of predictors using a physical system model specific to flat-panel cone-beam CT (FP-CBCT).

Methods: Physical models appropriate for integration with MBIR analysis are developed and parameterized to represent nonidealities in FP projection data including focal spot blur, scintillator blur, detector aperture effect, and noise correlations. Flat-panel-specific predictors for local spatial resolution and local noise properties in PL reconstructions are developed based on these realistic physical models. Estimation accuracy of conventional (idealized) and FP-specific predictors is investigated and validated against experimental CBCT measurements using specialized phantoms.

Results: Validation studies show that flat-panel-specific predictors can accurately estimate the local spatial resolution and noise properties, while conventional predictors show significant deviations in the magnitude and scale of the spatial resolution and local noise. The proposed predictors show accurate estimations over a range of imaging conditions including varying x-ray technique and regularization strength. The conventional spatial resolution prediction is sharper than ground truth. Using conventional spatial resolution predictor, the full width at half maximum (FWHM) of local point spread function (PSF) is underestimated by 0.2 mm. This mismatch is mostly eliminated in FP-specific prediction. The general shape and amplitude of local noise power spectrum (NPS) FP-specific predictions are consistent with measurement, while the conventional predictions underestimated the noise level by 70%.

Conclusion: The proposed image quality predictors permit accurate estimation of local spatial resolution and noise properties for PL reconstruction, accounting for dependencies on the system geometry, x-ray technique, and patient-specific anatomy in real FP-CBCT. Such tools enable prospective analysis of image quality for a range of goals including novel system and acquisition design, adaptive and task-driven imaging, and tuning of MBIR for robust and reliable behavior. [https://doi.org/10.1002/mp.13249]

Key words: CT image quality, flat-panel cone-beam CT, local point spread function, model-based iterative reconstruction, noise power spectrum

1. INTRODUCTION

Recent years have been increased use of flat-panel cone-beam CT (FP-CBCT) in both research and clinical settings. With a large and high-resolution detector, FP-CBCT can acquire volumetric information with a single rotation and can achieve submillimeter spatial resolution. These capabilities have made FP-CBCT popular for a number of clinical applications including small animal imaging,[1] three-dimensional (3D) breast imaging,[4–6] dental and maxillofacial studies,[2,3] and interventional procedures.[7–11]

Image quality assessment for FP-CBCT is an important element of system design, optimization, and quality control. A complete assessment evaluates the entire imaging chain including both acquisition and reconstruction stages. A wealth of literature has been devoted to *retrospective* image quality measurement wherein physical measurements (often of specialized phantoms) are collected and image quality metrics are subsequently computed based on an image reconstruction.[12,13] While retrospective assessment is valuable, it can be time-consuming to collect and reconstruct specialized data across a range of imaging conditions (e.g., different patient sizes, reconstruction parameters, etc.). Moreover, retrospective analysis is ill-suited to system design where hardware has not yet been constructed and physical data are unavailable.

Prospective performance analysis has been widely used in detector and imaging system design.[14,15] In particular, cascaded system analysis has been applied to model the end-to-end performance of FP-CBCT, modeling the important aspects of x-ray statistics, detection, and reconstruction. Characterizations have included the analysis of spatial resolution

and noise properties[16–18] as well as task-based metrics like detectability index that predict performance for specific clinical goals.[19] Such prospective methods have been used for CT system design including optimized hardware and geometry for FP-CBCT-based neuroimaging[20] and extremities imaging.[21] Similarly, prospective methods permit adaptive imaging where data acquisition is customized to the patient and diagnostic task, for example, adaptation of x-ray fluence[22,23] based on a predictive task-based performance metric.

Prospective analysis using cascaded systems has utilized highly sophisticated acquisition models of the source, detector, and scanner geometry. However, reconstruction models have focused largely on filtered-back projection (FBP). Model-based iterative reconstruction (MBIR) algorithms are now widely available on commercial CT scanners[24] and have become increasingly widespread in recent years due to improved tradeoffs between x-ray exposures and image quality.[25–31] MBIR achieves these advantages through the use of a detailed physical model, often including measurement statistics, as well as sophisticated regularization strategies to control noise.

In general, CT image quality is data-dependent and image properties are nonstationary. For example, like traditional FBP reconstruction, there are often noticeable differences in noise level and correlations throughout the image volume. While FBP tends to provide relatively uniform spatial resolution properties, MBIR tends to exhibit more complex data-dependent and shift-variant spatial resolution, in addition to nonstationary noise.[32] Thus, local image quality assessment within a small region and with respect to small intensity variations is important to capture overall performance. For example, spatial resolution properties may be measured locally using metrics like the local point spread function (PSF) or modulation transfer function (MTF).[33,34] Noise metrics such as local variance, spatial domain covariance, and noise power spectrum (NPS) have been computed for local region of interests (ROIs)[35,36] presuming local stationarity. Retrospective image quality assessment for MBIR is impotent to estimate through the complexities of data, location, and parameter dependence (e.g., regularization strength). Specifically, computing metrics like local PSF or NPS typically requires specific image features (e.g., a wire or edge, or uniform region in the object). Since MBIR has data-dependent image properties, metrics derived from a specialized phantom do not necessarily translate to patient data and are limited to regions where those features are present. This is in contrast to FBP where the underlying estimator is linear (though a nonlinear transformation of the data is required for transmission tomography) and it is easier to relate imaging performance between phantom and patient studies.

FBP has a closed-form expression of the reconstruction as a function of the measurements, which is convenient for theoretical analysis, permitting integration within an end-to-end cascaded model of a FP-CBCT system. In contrast, MBIR is typically defined implicitly as the optimizer of an objective function that is solved with iterative methods. Despite this, predictors for local spatial resolution and noise properties have been derived for one widely used class of MBIR — quadratically PL reconstruction. Such predictors are able to compute data-dependent and nonstationary local image properties based on knowledge of the system geometry, patient anatomy, and regularization.[37,38] Moreover, approximate expressions using Fourier methods have been derived for fast computation of local PSF and covariance.[39–41] These tools have found applications in regularization design to encourage uniform spatial resolution[42–44] or image properties optimized for specific tasks.[45] Similarly, such predictors have been used for task-driven adaptive imaging to optimize noncircular source–detector orbits[46,47] and dynamic x-ray fluence.[23,48]

While the prospective predictors discussed above have demonstrated utility in characterizing and controlling image properties, the system models are highly idealized. Specifically, conventional predictors for transmission tomography presume an idealized system without detector blur, source blur, or noise correlation between detector pixels. Exceptions to such idealizations include work in emission tomography on the influence of a radial detector blur on spatial resolution properties in PWLS reconstruction.[49] Related MBIR work has sought to develop improved system models for reconstruction of tomosynthesis data with correlated noise[50] and FP-CBCT data which exhibits source and detector blur as well as spatial correlations.[51] The importance of the high-fidelity models of source and detector in FP-CBCT cascaded systems analysis and successful integration of such models into MBIR suggests that improved image properties predictors are not only crucial for accurate performance evaluation but also feasible to derive and compute. In this work, we derive spatial resolution and noise predictors for the evaluation of quadratic PL performance wherein the reconstruction model is mismatched with the physical data acquisition. Specifically, a typical idealized system model is used in reconstruction while a more realistic data model is integrated into prospective image property predictors as part of the end-to-end system model. This corresponds to the common scenario in FP-CBCT, where a nonideal source and a detector constitute the imaging chain, but the MBIR data model is presumed to have Poisson noise, lacks a blur model, and neglects other nonidealities intrinsic to the real imaging chain.

Preliminary work in the development of FP-specific spatial resolution predictors showed significant improvements in the accuracy of local PSF[52] (especially in high-resolution applications). In this work, predictors for both spatial resolution and noise properties in PL reconstructions are developed, incorporating system blur and correlations specific to FP-CBCT. The predictors include parameterized models of source blur, detector scintillator blur, and aperture blur as well as flat-panel detector noise correlations. These physical parameters are estimated from FP-CBCT test bench measurements. This new set of FP-specific predictors is validated using phantom reference measurements on the same test bench. Accuracy of the predictors is assessed over a range of imaging scenarios including different x-ray techniques (including standard/low exposure levels, and with or without fluence modulation) and regularization strength. Initial results from these studies were presented in SPIE Medical

Imaging Conference (2018).[53] This work includes a complete and detailed mathematical derivation of the new predictors and additionally demonstrates the prediction accuracy across a greater variety of acquisition conditions (e.g., automatic exposure control).

2. METHODS

2.A. Flat-panel-specific CBCT system model

To develop image quality predictors for MBIR, one must have an accurate data model. The data model has two main elements: (a) the mean measurement model and (b) the noise model. The following subsections discuss each of these elements in detail.

2.A.1. Mean measurement model including system blur

There are two main physical sources of blur in FP-CBCT: (a) source blur from the finite size of the x-ray focal spot and (b) detector blur from physical effects including light spread in the scintillator and the aperture integration. One can express a full discretized monoenergetic acquisition model as

$$\bar{y}_{\text{acq}}(\mu) = \mathbf{S}\tilde{\mathbf{B}}_{\text{sc}} \sum_k \tilde{\mathbf{G}}_k \exp(-\tilde{\mathbf{A}}_k \mu) \tag{1}$$

where $\mu \in \mathbb{R}_+^N$ is a vector representing the attenuation volume with N voxels and $y \in \mathbb{R}_+^P$ is a vector of P projection measurements over detector elements and projection angles. Focal spot blur is modeled through a discretized sum over k sourcelets. For each sourcelet, $\tilde{\mathbf{A}}_k \in \mathbb{R}_+^{P_{\text{sub}} \times N}$ is the projection matrix defined on a fine virtual detector grid with P_{sub} subpixels total ($P_{\text{sub}} > P$). The gain term $\tilde{\mathbf{G}}_k$ models focal spot intensity variations for each sourcelet. Detector scintillator blur is denoted by the matrix $\tilde{\mathbf{B}}_{\text{sc}}$ and is applied to the finely sampled source-blurred signal, which is subsequently summed over physical detector pixels with the matrix $\mathbf{S} \in \mathbb{R}^{P \times P_{\text{sub}}}$, modeling the detector pixel aperture function.

However, the model above involves a fairly complicated formulation that is not well suited to fast implementation of image property predictors. Following related work,[54] one can make a series of approximations to rewrite the acquisition model in a form without the sum over sourcelets. Specifically, we write the model as

$$\bar{y}_{\text{acq}}, j(\mu) \approx \mathbf{B}_{\text{sc}} \mathbf{B}_{\text{fs}}^j I_0 \exp(-\mathbf{A}\mu) \tag{2}$$

using a standard (non-sourcelets) projection matrix, $\mathbf{A} \in \mathbb{R}_+^{P \times N}$, and individual models of detector scintillator blur and source blur effects with

$$\mathbf{A} \approx \mathbf{S}\left[\tilde{\mathbf{L}}_k^j\right]^{-1} \tilde{\mathbf{A}}_k \tag{3}$$

$$\mathbf{B}_{\text{sc}} = \frac{1}{d}\mathbf{S}\tilde{\mathbf{B}}_{\text{sc}}\mathbf{S}^T \tag{4}$$

$$\mathbf{B}_{\text{fs}}^j = \frac{1}{dI_0} \sum_k \mathbf{S}\tilde{\mathbf{G}}_k \tilde{\mathbf{L}}_k^j \mathbf{S}^T. \tag{5}$$

In the above expressions, $\mathbf{S}^T$ denotes an upsampling operation, d is the number of virtual subpixels per pixel (based on the original model), I_0 represents an average x-ray fluence level (x-ray quanta/detector pixel), and $\tilde{\mathbf{L}}_k^j$ is a sourcelet-specific shift operator. The shift operator uses the assumption that neighboring sourcelet rays may be approximated by a simple shift and (weighted) sum of projection values. Since focal spot blur is depth dependent (i.e., dependent on the position of the object with respect to the source and detector), the amount of shift varies by position in the field of view (as indicated by index j). Note that the detector aperture is now included in $\mathbf{A}$ via the downsampling operator $\mathbf{S}$ within the exponent of the forward model. For the blur operators, $\mathbf{B}_{\text{sc}}$ is a resampled version of detector scintillator blur $\tilde{\mathbf{B}}_{\text{sc}}$ that is applied directly to the sampled projection image on the detector pixel grid, and $\mathbf{B}_{\text{fs}}^j$ approximates local source blur as an additional projection blur. A complete focal spot model can be obtained by experimentally measuring the system blur using a test object at multiple positions or through shape models of the focal spot on the anode of the x-ray tube.[55]

We can further simplify the acquisition model by approximating focal spot blur and considering the source blur exhibited by one point in the field of view, for example, the center of the field of view. Defining $\mathbf{B} = \mathbf{B}_{\text{sc}}\mathbf{B}_{\text{fs}}^{\text{center}}$ then permits us to write:

$$\bar{y}_{\text{acq,FP}}(\mu) = \mathbf{B} I_0 \exp(-\mathbf{A}\mu). \tag{6}$$

We will use this mathematically compact model in subsequent derivations of local resolution predictor; however, we note that it is straightforward to use the shift-variant blur model of Eq. (2) as well. Again, note that the blur kernel $\mathbf{B}$ does not contain aperture blur, which is included in the projector $\mathbf{A}$ using the separable footprints method.[56]

2.A.2. Measurement noise model

CT measurements are often regarded as independent with a Poisson or Gaussian distribution. However, the independence assumption is not necessarily suited to flat-panel detector modeling. In indirect detectors, a scintillator absorbs primary x-ray photons and converts the energy to hundreds or thousands of visible light photons. These light photons can spread within the scintillator and are, in turn, converted to an electronic signal by the detector. The statistics of the secondary quanta are somewhat complex, combining a compound Poisson noise process with spatial correlations. Rabbani et al. theoretically analyzed the behavior of stochastic amplification and scattering mechanisms in imaging systems and developed a stochastic blur model.[57] Such models have been validated in flat-panel detector experiments[58,59] and are appropriate for local noise analysis. We adopt the following model from cascaded system analysis:[60]

$$S_{\text{det}} = a_{\text{pd}}^4 \bar{q}_0 \bar{g}_1 \bar{g}_2 \bar{g}_4 \left[1 + \bar{g}_4 P_K T_3^2\right] T_{\text{a}}^2 + S_{\text{ro}} \tag{7}$$

where S_{det} is the NPS flat-panel detector neglecting aliasing, and $\bar{q}_0$ is the mean of primary x-ray quanta. The factors $\bar{g}_1, \bar{g}_2, \bar{g}_4$ are the average gains for x-ray photon interaction, optical conversion, and coupling stages, respectively. The transfer function T_3 accounts for optical photon spread, and P_K is the transfer function associated with *K*-fluorescence.[61] Scintillator blur may be defined as $T_{\text{sc}} = T_3\sqrt{P_K/P_K(0)}$ accounting for both optical photon and k-fluorescence spread. The aperture MTF is denoted by T_{a}, a_{pd} is the aperture size, and S_{ro} is the additive readout electronic NPS. The magnitude of the quantum NPS ($S_{\text{det}} - S_{\text{ro}}$) is proportional to the incident quanta $\bar{q}_0$. The quanta-normalized NPS ($(S_{\text{det}} - S_{\text{ro}})/q_0$) is independent of total fluence and has a fixed profile. Noise can be generally categorized into noise that is correlated via the scintillator transfer function T_{sc}, and noise that remains uncorrelated. Thus, we parameterize the noise model using two factors G_0 and γ_{c} that summarize the noise propagation in the detector:

$$S_{\text{det}} = \bar{q}_0 G_0 \left[1 + \gamma_{\text{c}} T_{\text{sc}}^2\right] T_{\text{a}}^2 + S_{\text{ro}}. \tag{8}$$

with the total gain $G_0 = a_{\text{pd}}^4 \bar{g}_1 \bar{g}_2 \bar{g}_4$ and a factor that characterizes the amount of noise that is correlated, $\gamma_{\text{c}} = \bar{g}_4 P_K(0)$. This noise model will be used in the local noise predictor derivations.

2.A.3. Reconstruction models and penalized-likelihood estimation

In this work, we focus on PL estimation of attenuation coefficients. The PL estimator is defined implicitly as the optimizer of an objective function. Generally, there is no closed-form solution, so the estimate is approximated iteratively. Mathematically, we may write

$$\hat{\mu}(y) = \arg\max_{\mu} \Phi(\mu; y) \tag{9}$$

where $\hat{\mu} \in \mathbb{R}_+^N$ is the estimate of attenuation coefficients based on noisy projection data $y \in \mathbb{R}_+^P$. The PL objective function $\Phi(\mu;y)$ combines a statistical data fidelity term based on the log-likelihood $L(\mu;y)$ with a roughness penalty term $R(\mu)$.

$$\Phi(\mu; y) = L(\mu; y) - \beta R(\mu) \tag{10}$$

The penalty term attributes higher cost for large local image differences to encourage smoothness. The relative balance between data fidelity and regularization is controlled by the scalar, β. In this work, we focus on a quadratic roughness penalty with the first-order neighborhood and pairwise voxel differences written as

$$R(\mu) = \sum_j \sum_{k \in \mathcal{N}_j} \frac{1}{2} (\mu_j - \mu_k)^2 \tag{11}$$

where $\mathcal{N}_j$ denotes a neighborhood of voxels around location *j*.

As mentioned previously, PL methods often adopt independent Poisson models for measurements. In this case, the data fidelity term can be expressed as a sum over measurements, *i*, with

$$L(\mu; y) = \sum_i y_i \log[\bar{y}_{\text{recon}}(\mu)]_i - [\bar{y}_{\text{recon}}(\mu)]_i. \tag{12}$$

Again, the traditional mean measurement model for reconstruction, $\bar{y}_{\text{recon}}(\mu)$, ignores system blur and uses the following simple transmission model:

$$\bar{y}_{\text{recon}}(\mu) = I_0 \exp(-\mathbf{A}\mu) \tag{13}$$

We note the explicit differences between the more accurate physical model of acquisition in Eq. (6) and the idealized reconstruction model in Eq. (13). These mismatched models are indicated by the subscripts on *y*. Similarly, the independent and Poisson noise model implicit in the log-likelihood in Eq. (12) is mismatched with the correlated noise model of Eq. (8).

2.B. Image properties prediction

2.B.1. Local spatial resolution predictors

Previous studies have shown that PL reconstructions yield shift-variant resolution properties. However, such resolution properties are locally linear and locally shift-invariant with quadratic roughness penalties.[39] In this case, analysis using local PSFs is appropriate for image quality assessment. The local PSF is defined as the expected relative change in the reconstruction image when a small local impulse is introduced into the image volume. Mathematically, the local PSF may be written as

$$\begin{aligned} \text{PSF}_j &= \lim_{\delta \to 0} \frac{1}{\delta} \left[\hat{\mu}\left(\bar{y}_{\text{acq}}\left(\mu + \delta e_j\right)\right) - \hat{\mu}\left(\bar{y}_{\text{acq}}(\mu)\right)\right] \\ &= \frac{\partial}{\partial \mu_j} \hat{\mu}\left(\bar{y}_{\text{acq}}(\mu)\right) \end{aligned} \tag{14}$$

Note that this expression can be interpreted as a difference between PL reconstructions of noiseless projection data based on objects with and without a small local impulse change at location *j*. The magnitude of change is denoted by scalar δ, e_j denotes a vector representing a Kronecker delta with unity in the *j* element, and μ_j is the j^{th} element of image vector μ. Following previous work[39] and applying the chain rule, we can separate the local PSF into two factors:

$$\frac{\partial}{\partial \mu_j} \hat{\mu}\left(\bar{y}_{\text{acq}}(\mu)\right) = \frac{\partial}{\partial \mu_j} \bar{y}_{\text{acq}}(\mu) \cdot \nabla_{\bar{y}_{\text{recon}}} \hat{\mu}(\bar{y}_{\text{recon}}(\mu)) \tag{15}$$

The first term is a derivative of the acquisition model for physical signal propagation. Previously derived local PSF estimators used an acquisition model matched to the reconstruction model such that

$$\frac{\partial}{\partial \mu_j} \bar{y}_{\text{acq,ideal}} = -\mathbf{D}\{I_0 \exp(-\mathbf{A}\mu)\}\mathbf{A}e_j \tag{16}$$

where $\mathbf{D}[\cdot]$ denotes the operator that places the argument of a vector in $\mathbb{R}^N$ along the main diagonal of a matrix in $\mathbb{R}^{N \times N}$.

Using the more sophisticated acquisition model in Eq. (6), one finds

$$\frac{\partial}{\partial \mu_j}\bar{y}_{\text{acq,FP}} = -\mathbf{BD}\{I_0 \exp(-\mathbf{A}\mu)\}\mathbf{A}e_j. \tag{17}$$

Note that the difference between the old and new terms is in the addition of the system blur operator in Eq. (17).

The second term in Eq. (15) is a gradient of the estimator with respect to the measurements. This term relies on the measurement model for reconstruction in Eq. (13) and may be written as

$$\begin{aligned}&\nabla_{\bar{y}_{\text{recon}}}\hat{\mu}(\bar{y}_{\text{recon}}(\mu))\\ &= -\left[\mathbf{A}^T\mathbf{D}\{I_0 \exp(-\mathbf{A}\hat{\mu}(y))\}\mathbf{A} + \mathbf{R}\right]^{-1}\mathbf{A}^T\end{aligned} \tag{18}$$

where $\mathbf{R} = \nabla^2 R(\mu)$ is the Hessian of the penalty term.

In Eqs.(16-18), diagonal weighting terms are based on idealized projections of the true attenuation volume or of the reconstruction of measurement data. It is important to note that the dependencies on patient anatomy and x-ray technique are introduced through this diagonal weighting term. Moreover, the expression depends only on the object through projections of the object. Thus, even if ground truth volumes are not generally available, we can approximate these weights with the measurements themselves, $\mathbf{W} = D\{y\}$.[39] Thus, we can express traditional and FP-specific resolution predictors as

$$\text{PSF}_j^{\text{ideal}} = \left[\mathbf{A}^T\mathbf{WA} + \mathbf{R}\right]^{-1}\mathbf{A}^T\mathbf{WA}e_j \tag{19}$$

$$\text{PSF}_j^{\text{FP}} = \left[\mathbf{A}^T\mathbf{WA} + \mathbf{R}\right]^{-1}\mathbf{A}^T\mathbf{BWA}e_j. \tag{20}$$

Note that the difference between these resolution predictors lies in the right-hand side of the expressions where the Fisher information term $\mathbf{A}^T\mathbf{WA}$ derived from the reconstruction process is mismatched with $\mathbf{A}^T\mathbf{BWA}$ that also contains the system blur operator.

To avoid the computational complexity of matrix inverses in Eqs. (19) and (20), Fourier approximation in a local ROI around j may be applied to accelerate prediction. This results in the following closed-form predictors:

$$\text{PSF}_j^{\text{ideal}} = \mathscr{F}^{-1}\left\{\frac{\mathscr{F}\{\text{ROI}_j\{\mathbf{A}^T\mathbf{WA}e_j\}\}}{\mathscr{F}\{\text{ROI}_j\{\mathbf{A}^T\mathbf{WA}e_j + \mathbf{R}e_j\}\}}\right\} \tag{21}$$

$$\text{PSF}_j^{\text{FP}} = \mathscr{F}^{-1}\left\{\frac{\mathscr{F}\{\text{ROI}_j\{\mathbf{A}^T\mathbf{BWA}e_j\}\}}{\mathscr{F}\{\text{ROI}_j\{\mathbf{A}^T\mathbf{WA}e_j + \mathbf{R}e_j\}\}}\right\} \tag{22}$$

where $\mathscr{F}$ and $\mathscr{F}^{-1}$ denote the discrete Fourier transform and inverse transform, respectively, and $\text{ROI}_j\{\cdot\}$ denotes taking a cubic ROI centered at the j^{th} voxel. Note that both predictors may be computed given projection data alone (via $\mathbf{W}$) without the need for explicit reconstruction. Moreover, the expression above captures the dependencies on patient anatomy, exposure, geometry, regularization, and location. Performance of both predictors will be evaluated and compared in this work.

2.B.2. Local noise predictors

Various noise metrics are often used in CT image quality assessments. While simple measures of variance are often used for the purposes of basic quality or consistency checks, NPS or covariance metrics are desirable since they quantify the structure and frequency content of the noise. In PL reconstruction, noise properties are generally nonstationary; however, quadratic penalties generally induce smooth variations in noise statistics. Thus, we can assume local stationarity within reasonably small ROIs to facilitate noise analysis.

Following previous work,[39] we derive the first-order Taylor expansion of a PL reconstruction about noise-free projections such that

$$\hat{\mu}(y) \approx \hat{\mu}(\bar{y}) + \nabla_{\bar{y}_{\text{recon}}}\hat{\mu}(\bar{y}_{\text{recon}}(\mu))(y - \bar{y}_{\text{acq}}). \tag{23}$$

Note the mismatch between acquisition and reconstruction forward models. Taking the covariance of both sides, one finds

$$\text{Cov}\{\hat{\mu}\} = \nabla_{\bar{y}_{\text{recon}}}\hat{\mu}(\bar{y}_{\text{recon}}(\mu))\text{Cov}\{y_{\text{acq}}\}\left[\nabla_{\bar{y}_{\text{recon}}}\hat{\mu}(\bar{y}_{\text{recon}}(\mu))\right]^T \tag{24}$$

where $\text{Cov}\{y\}$ is the covariance of noisy measurements. The term $\nabla_{\bar{y}}\hat{\mu}(\bar{y}(\mu))$ represents noise propagation through reconstruction based on the idealized forward model $\bar{y} = \bar{y}_{\text{recon}}$ which was previously stated in Eq. (18).

The local covariance between $\hat{\mu}_j$ and the entire image volume $\hat{\mu}$ is represented by the j^{th} column of the covariance matrix $\text{Cov}\{\hat{\mu}\}$. That is,

$$\text{Cov}\{\hat{\mu}, \hat{\mu}_j\} = \text{Cov}\{\hat{\mu}\}e_j \tag{25}$$

Under the conventional assumption of CT measurements that are presumed to be statistically independent with variance equal to their mean (e.g., Poisson distributed). The covariance matrix for ideal measurements is a diagonal matrix

$$\text{Cov}\{y\} = \mathbf{D}\{\bar{y}_{\text{acq}}\} \approx \mathbf{W} \tag{26}$$

Thus, an idealized predictor of covariance may be written as

$$\begin{aligned}&\text{Cov}^{\text{ideal}}\{\hat{\mu}, \hat{\mu}_j\}\\ &= \left[\mathbf{A}^T\mathbf{WA} + \mathbf{R}\right]^{-1}\mathbf{A}^T\mathbf{WA}\left[\mathbf{A}^T\mathbf{WA} + \mathbf{R}^T\right]^{-1}e_j\end{aligned} \tag{27}$$

This model ignores the more sophisticated FP detector noise model in Eq. (8). To use the FP model, one must estimate the locally incident primary x-ray photons $\bar{q}_0$ and the general detector gain term G_0. However, the projection data including the simplified I_0 factor in the reconstruction model is proportional to the total detector response $\bar{q}_0 G_0$ in a locally uniform region. An empirical gain term G is introduced to account for the conversion between the primary x-ray photon distribution and projection data. Details of the Poisson equivalent fluence I_0 calculation and the relationship between gain terms in both models are described in Appendix A. With the

empirical gain G and reconstruction model, the local detector NPS (in the absence of aliasing) can be written as

$$S_{\text{det}}, i = G[I_0 \exp(-[\mathbf{A}\mu]_i)][1 + \gamma_c T_{\text{sc}}^2]T_a^2 + S_{\text{ro}} \tag{28}$$

where $[\mathbf{A}\mu]_i$ denotes the line integral associated with the i^{th} measurement. Presuming local stationarity, it is straightforward to find a covariance function using the inverse Fourier transform. To model structured projection data, we presume that the predetection signal is globally nonuniform, independent, Poisson distributed, and locally smooth. Under this local stationarity assumption, we take the inverse Fourier transform of Eq. 28 and write the following model:

$$\text{Cov}^{\text{FP}}\{y\} = \frac{1}{a_u a_v}[\mathbf{B}_{\text{a}}(\gamma_c \mathbf{B}_{\text{sc}} G\mathbf{W}\mathbf{B}_{\text{sc}}^T + G\mathbf{W})\mathbf{B}_{\text{a}}^T + \mathbf{K}_{\text{ro}}]. \tag{29}$$

Here, $\mathbf{B}_{\text{a}}$ is the aperture blur, $\mathbf{K}_{\text{ro}}$ denotes the additive electronic noise covariance matrix, and a_u, a_v are the detector pixel sizes along u,v direction, respectively.

Combining Eqs. (19) and (29) into (25) yields

$$\text{Cov}^{\text{FP}}\{\hat{\mu}, \hat{\mu}_j\} = \left[\mathbf{A}^T\mathbf{W}\mathbf{A} + \mathbf{R}\right]^{-1}\mathbf{A}^T\text{Cov}^{\text{FP}}\{y\}\mathbf{A}\left[\mathbf{A}^T\mathbf{W}\mathbf{A} + \mathbf{R}^T\right]^{-1}e_j. \tag{30}$$

Again, the idealized and FP-specific noise predictions may be computed with Fourier methods. Moreover, if one wishes to focus on the local NPS instead of local covariance, there is no need for an inverse Fourier transform operation. As such, we arrive at the following idealized and FP-specific predictors for local NPS:

$$\text{NPS}_j^{\text{ideal}} = \frac{\mathscr{F}\{\text{ROI}_j\{\mathbf{A}^T\mathbf{W}\mathbf{A}e_j\}\}}{\left[\mathscr{F}\{\text{ROI}_j\{\mathbf{A}^T\mathbf{W}\mathbf{A}e_j + \mathbf{R}e_j\}\}\right]^2} \tag{31}$$

$$\text{NPS}_j^{\text{FP}} = \frac{\mathscr{F}\{\text{ROI}_j\{\mathbf{A}^T\left[G\mathbf{B}_{\text{a}}(\gamma_c\mathbf{B}_{\text{sc}}\mathbf{W}\mathbf{B}_{\text{sc}}^T + \mathbf{W})\mathbf{B}_{\text{a}}^T + \mathbf{K}_{\text{ro}}\right]\mathbf{A}e_j\}\}}{a_u a_v\left[\mathscr{F}\{\text{ROI}_j\{\mathbf{A}^T\mathbf{W}\mathbf{A}e_j + \mathbf{R}e_j\}\}\right]^2}. \tag{32}$$

Note that the difference lies in the numerators as derivations from the idealized or FP-specific acquisition noise models. Again, object dependency is captured in both of these expressions through the data weighting term, $\mathbf{W} = D\{y\}$. As with the resolution predictors, both of the above expressions may be computed without explicit reconstruction and encompass dependencies on not only patient anatomy but also exposure, geometry, regularization, and location.

2.C. Validation of predictors in physical experiments

2.C.1. FP-CBCT system characterization

In this work, we evaluated predictors of spatial resolution and noise on a CBCT test bench shown in Fig. 1(a). The bench includes an x-ray tube (Varian Rad-94 Sappire) and a flat-panel detector (Varex PaxScan 4343CB, 1536 × 1536 pixels, pixel size 0.278 mm × 0.278 mm, fill factor $\gamma_{\text{pix}} = 60.7\%$). The system geometry was identical for all scans with source-to-axis distance of 912 mm and source-to-detector distance of 1150 mm.

Characterization and validation of the underlying system blur and flat-panel detector noise models are essential before validation of the predictors of reconstructed FP-CBCT image properties. To this end, system blur associated with the detector and x-ray focal spot was estimated. As in previous work,[62] we used a tungsten plate (50 mm × 50 mm × 5 mm) with a sharp, straight edge to measure detector blur. A presampled edge response function (ESF) was estimated by interleaving 200 edge measurements along the angled edge and differentiated to obtain a one-dimensional (1D) line spread function (LSF). Fourier transformation of the 1D-LSF yields the MTF associated with the direction perpendicular to the edge. The tungsten plate was placed along different orientations to evaluate MTF along different directions (e.g., a possibly anisotropic detector blur). To measure the effects of focal spot blur, the tungsten plate was placed at axis-of-rotation (e.g., the center of the field of view) to measure the total system blur. We note that the source blur effects can be isolated by dividing the total blur MTF by the detector MTF, though the

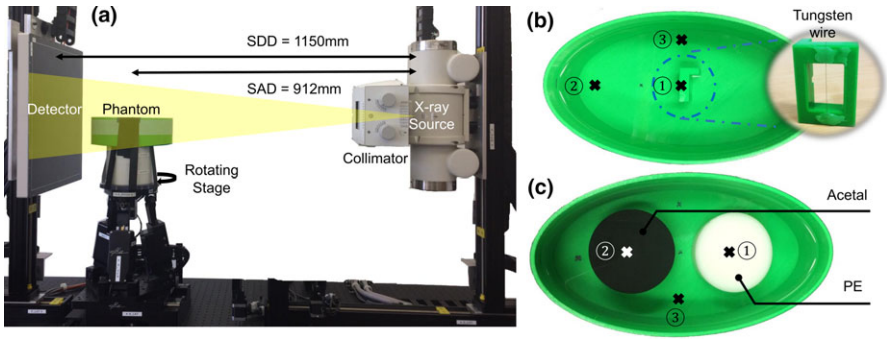

FIG. 1. Materials used in physical experiments including: (a) the CBCT test bench setup. (b) The resolution phantom with a positionable tungsten wire. Resolution properties at three positions (marked with crosses) were investigated. (c) The noise phantom with two uniform cylindrical inserts. Noise properties in three uniform materials (polyethylene, acetal, and water) were investigated. [Color figure can be viewed at wileyonlinelibrary.com]

source blur alone is not required for the predictor models.The aperture blur is divided out to fit the blur kernel in derivations, characterized by detector parameters (pixel size and fill factor), and modeled by a 2D sinc function using

$$T_a(f_u,f_v) = \left|\mathrm{sinc}(\sqrt{\gamma_{\mathrm{pix}}}a_u f_u)\mathrm{sinc}(\sqrt{\gamma_{\mathrm{pix}}}a_v f_v)\right| \quad (33)$$

For flat-panel noise modeling, the 2D detector NPS was measured using six flat fluence exposures.[58] Each set of data was gain and offset corrected, and was multiplied by fluence intensity I_0 presuming uniform fluence field at each view, which was estimated by computing the mean divided by the variance (over an ROI) to yield the number of noise equivalent photons to match the Poisson reconstruction model. The readout noise S_{ro} was measured in dark images and subtracted. Estimates of NPS were divided by I_0 which normalized the area under the spectrum and divided by T_a^2 to eliminate detector aperture effect. Since we observed that the area-normalized presampled 2D NPS $((S_{\mathrm{det}} - S_{\mathrm{ro}})/(I_0 T_a^2))$ was highly isotropic, each was radially averaged for noise reduction.

The scintillator MTF was calculated by dividing the detector MTF (as estimated from edge responses) by the aperture MTF. The parameters G and γ_c from the detector noise model in Eq. (28) were determined by linear regression fitting of area-normalized presampled NPS profiles to the squared 1D scintillator MTF.

2.C.2. Data acquisition and reconstruction

To investigate the accuracy of the resolution and noise predictors, local PSF and NPS estimates were computed in reconstructed images of specialized phantoms and an anthropomorphic chest phantom. The measurements are compared with the analytical predictions as references.

We used a water-filled 3D-printed phantom [Figs. 1(b) and 1(c)] to emulate typical patient quantum noise variations (e.g., in a thorax) as a function of projection angle. The phantom was elliptical with a major axis of 26 cm and minor axis of 14 cm. Different inserts were used for the spatial resolution and noise predictor validations, and are discussed in the following sections.

In the specialized phantom experiments, two technique protocols commonly employed in FP-CBCT systems were investigated. Specifically, we considered two x-ray exposure techniques:

(1) Unmodulated x-ray technique. The tube current was constant for all frames at a reference exposure level.
(2) Automatic exposure control (AEC). The approximately constant fluence at the center of the detector[63] at a quarter of reference dose level was delivered. On the FP-CBCT test bench, AEC was achieved by pulse width modulation to control the mAs/frame. (Other CT systems achieve the same effect via tube current modulation.)

In addition to the specialized phantoms, a custom anthropomorphic chest phantom (Fig. 3) with human bone and tissue-equivalent plastic was used to verify the prediction accuracy in a more realistic case. In the anthropomorphic phantom scans, only the unmodulated x-ray technique was applied.

The PL reconstruction algorithm was coded in MATLAB with external calls to CUDA-based libraries implementing separable footprints projectors and backprojectors. The separable paraboloidal surrogates (SPS) algorithm[64] was chosen to minimize the PL objective function Eq. (13) with quadratic penalty design as in Eq. (11). Curvature precomputation[65] and varying numbers of ordered subsets (18 subsets for the first 50 iterations, 10 subsets for the following 50 iterations, and 1 subset for 500 iterations)[66] were used to ensure highly converged solutions with 600 iterations total. Images were reconstructed using a $750 \times 1350 \times 200$ volume with 0.2 mm cubic voxels.

Fluence levels (I_0) were estimated as discussed in Section 2.C.1. For unmodulated scans, I_0 was 6.0×10^4 photons/pixel for the specialized phantom experiments and 7.7×10^4 photons/pixel for the anthropomorphic phantom experiments; for AEC scans, I_0 changed from frame to frame as shown in Fig. 2, but was approximately 1.5×10^4 photons/pixel averaged over all frames. All projection data used 360 projection frames equally spaced over 360°. Varying regularization strengths β between 10^4 and $10^{6.5}$ were investigated to leverage between the data fidelity term and image roughness penalty term.

2.C.3. Spatial resolution predictor validation

In spatial resolution studies, a tungsten wire [Fig. 1(b)] was used as a resolution probe.[67] The wire was thin (ϕ = 127 μm smaller than the voxel size), making it a good physical approximation to a local impulse. The wire was immersed in water or in casting resin to emulate surrounding attenuation from patient anatomy. To estimate a local PSF, a local ROI in the reconstructed volume ($71 \times 71 \times 51$ voxels) including the wire was selected. A background water attenuation value was calculated using an annulus surrounding the

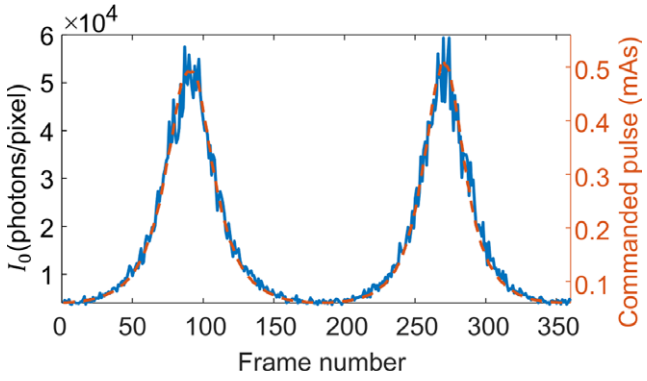

FIG. 2. Tube current modulation profiles. [Color figure can be viewed at wileyonlinelibrary.com]

wire and subtracted from the ROI. The wire center in 20 consecutive slices was estimated using Gaussian fitting to align slices with subpixel translation. The 2D wire response $\mathrm{PSF}^{\mathrm{wire}}(x,y)$ was approximated by interleaving samples from the centered slices. Blur due to the 2D wire response was removed using a wire cross section model ($f_{\mathrm{wire}}(x,y)$, equal to a disc with diameter ϕ = 127 mm) via Fourier methods. After normalization, a 2D in-plane PSF estimate was achieved.

To compare measured PSF values with the predictor requires forming a similar 2D in-plane PSF from the 3D PSF prediction. Specifically, the 2D in-plane PSF corresponds to an integral of the 3D PSF over the axial direction. Thus, the following integration was computed using a finite sum over PSF samples:

$$\mathrm{PSF}^{\mathrm{pred}}(x,y) = \int_z \mathrm{PSF}^{\mathrm{pred}}(x,y,z)dz. \tag{34}$$

The spatial resolution predictor was validated at the three locations marked with crosses in Fig. 1(b). This was achieved with the wire probe fixed at each location in three scans. Both unmodulated and AEC x-ray techniques were applied for each set of acquisitions.

Influence of regularization strength was investigated through varying *beta*. The FWHM was calculated by averaging the diameter of the half-maximum contour of the 2D PSF. In each reconstruction, multiple samples of measured PSFs were calculated, each integrating ten slices at varying z locations.

2.C.4. Local noise predictor validation

For noise validation studies, two uniform cylinders (ϕ 77 mm × H 40 mm) made of polyethylene and acetal were inserted in the elliptical phantom (Fig. 1). In the anthropomorphic phantom, the noise properties are investigated in two locally uniform locations [see Fig. 3(a)]. Two scans were acquired, reconstructed, and subtracted to form a noise-only image volume. Presuming local stationarity, a local 3D NPS was calculated using a sliding window technique with nine 3D ROIs, each 71 × 71 × 31 voxels, aligned axially, and half-overlapped in the z-direction. The NPS was computed as

$$\mathrm{NPS}(f_x,f_y,f_z) = \frac{1}{2}\frac{a_x a_y a_z}{n_x n_y n_z}\langle|\mathrm{DFT}[\Delta\mathrm{ROI}(x,y,z)]|^2\rangle \tag{35}$$

where a is the voxel size and n_x, n_y, and n_z are the number of voxels in each direction of the ROI. The 3D NPS predictions were compared with estimates based on measurements and the central NPS slices ($f_z = 0$) are displayed.

Local noise estimates and prediction were compared at three selected locations marked with crosses in Fig. 1. Each location was within a uniform region (though each material — polyethylene, water, acetal had a different mean attenuation). Both unmodulated and AEC x-ray techniques were investigated and two regularization parameters were applied.

3. RESULTS

3.A. FP-CBCT system characterization

The results of CBCT system blur characterization are shown in Fig. 4. Detector blur estimates consist of the scintillator blur and the aperture blur given by 1D-MTFs over five orientations. No significant angular differences were observed. Investigation at different locations on the panel (not shown) obtained nearly identical 1D-MTF curves, suggesting that the detector response was also highly shift-invariant (e.g., obliquity effects were not significant for this geometry). We found that FWHM of 2D detector blur kernel was approximately 0.37 mm. The total blur measured with the edge at the axis of rotation is only slightly blurrier than detector blur suggesting limited focal spot blur with a total system blur FWHM of approximately 0.40 mm. In all studies, we used a focal spot whose size was nominally 0.4. With a system magnification of 1.26 and anode size smaller, the expected FWHM of focal spot blur should be less than 0.1 mm. With the total system blur dominated by scintillator blur, the system is approximated well using a shift-invariant approximation (though one could also incorporate a shift-variant model for the focal spot blur). In following estimations, the aperture MTF is divided out from the total blur to fit the

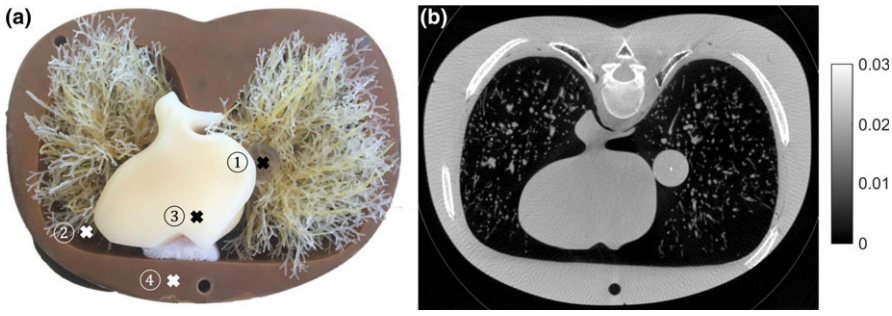

FIG. 3. (a) The custom anthropomorphic chest phantom including a Kyoto Kagaku "Lungman" insert emulating the cardiac region and lungs. A tungsten wire cast in a polyester background was inserted at positions 1 and 2 for spatial resolution properties investigations. Noise properties are investigated at positions 3 and 4 using the difference of two repeated scans. (b) The CT axial image of the anthropomorphic phantom with tungsten wire inserted. [Color figure can be viewed at wileyonlinelibrary.com]

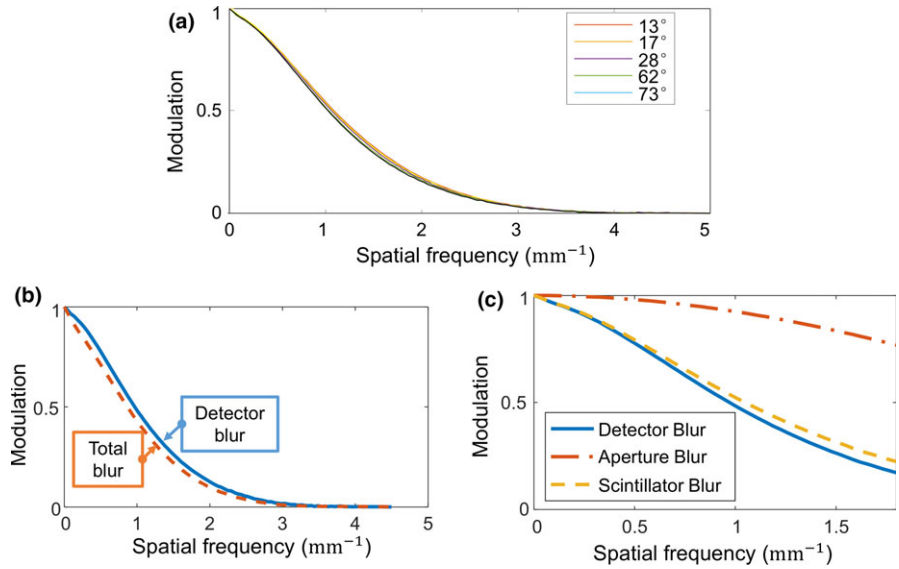

FIG. 4. Flat-panel detector and CBCT system resolution properties measurement. (a) Detector MTF for five orientations, (b) MTF of detector blur and total system blur, (c) Detector blur, aperture blur, and scintillator blur within the Nyquist frequency. [Color figure can be viewed at wileyonlinelibrary.com]

estimation model, where the **B** is the combination of the scintillator blur and the source blur.

Detector NPS was measured for six exposure levels with a uniform bare beam. Readout NPS was estimated as a constant and subtracted from detector NPS. The readout-noise-free detector NPS was divided by T_a^2 to eliminate the aperture effect. Normalized by area, each 2D NPS map of scintillator photons was highly isotropic.

Angularly averaged profiles are shown in Fig. 5(a). Using the detector blur measurements and the averaged NPS profile, we used linear regression to estimate parameters γ_c and G in the stochastic blur model Eq. (8). We found that $\gamma_c = 7.52$ and $G = 0.032$ mm^2 optimized the parameteric model. The data fit is found as shown in Fig. 5(b) with root-mean-square error 1.9×10^{-3}mm^2. These parameters and scintillator/aperture MTF estimates were used in subsequent predictor validation studies.

3.B. Local spatial resolution predictor validation

A summary of the spatial resolution validation in specialized phantom studies is shown in Fig. 6. Each row shows PSF predictions with an idealized and flat-panel-specific predictor as well as estimates based on physical measurements. Each column shows the local PSF in a different phantom location. Line plots below compare central profiles of local PSF measurements and predictions in both horizontal and vertical directions at the corresponding position. Unmodulated scan results are shown on the left, while AEC results are on the right. In both cases, the PL regularization parameter was $\beta = 10^5$.

Both unmodulated and AEC experiments show similar results in terms of PSF prediction accuracy. Namely, the predicted PSF using the flat-panel CBCT-specific model closely matches measured PSF results. This is apparent both in the 2D PSF images as well as the 1D profiles. In contrast, the idealized predictor underestimated blur in the reconstruction. This is unsurprising since the idealized mode does not account for flat-panel detector blur nor focal spot blur. The underestimation is most easily seen in the profile plots.

A number of other interesting trends are apparent in these results. We see that measured local PSF estimates vary across positions, illustrating strong shift-variant resolution properties in PL reconstruction. The proposed predictor successfully captures these features and shows a good match in all three positions. The largest mismatch is identified at the

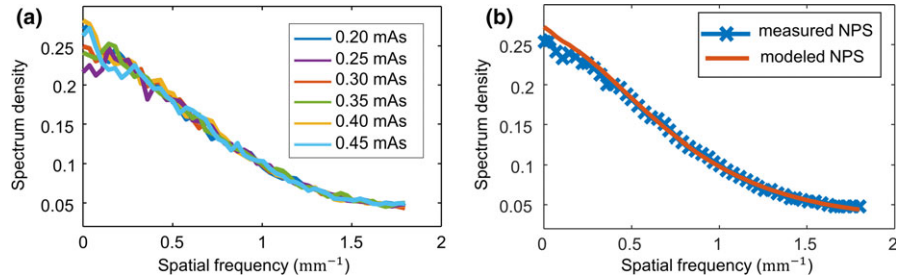

FIG. 5. Flat-panel detector noise properties measurement. (a) Normalized averaged NPS profiles at six exposure levels, (b) Measured and modeled area-normalized NPS profiles. [Color figure can be viewed at wileyonlinelibrary.com]

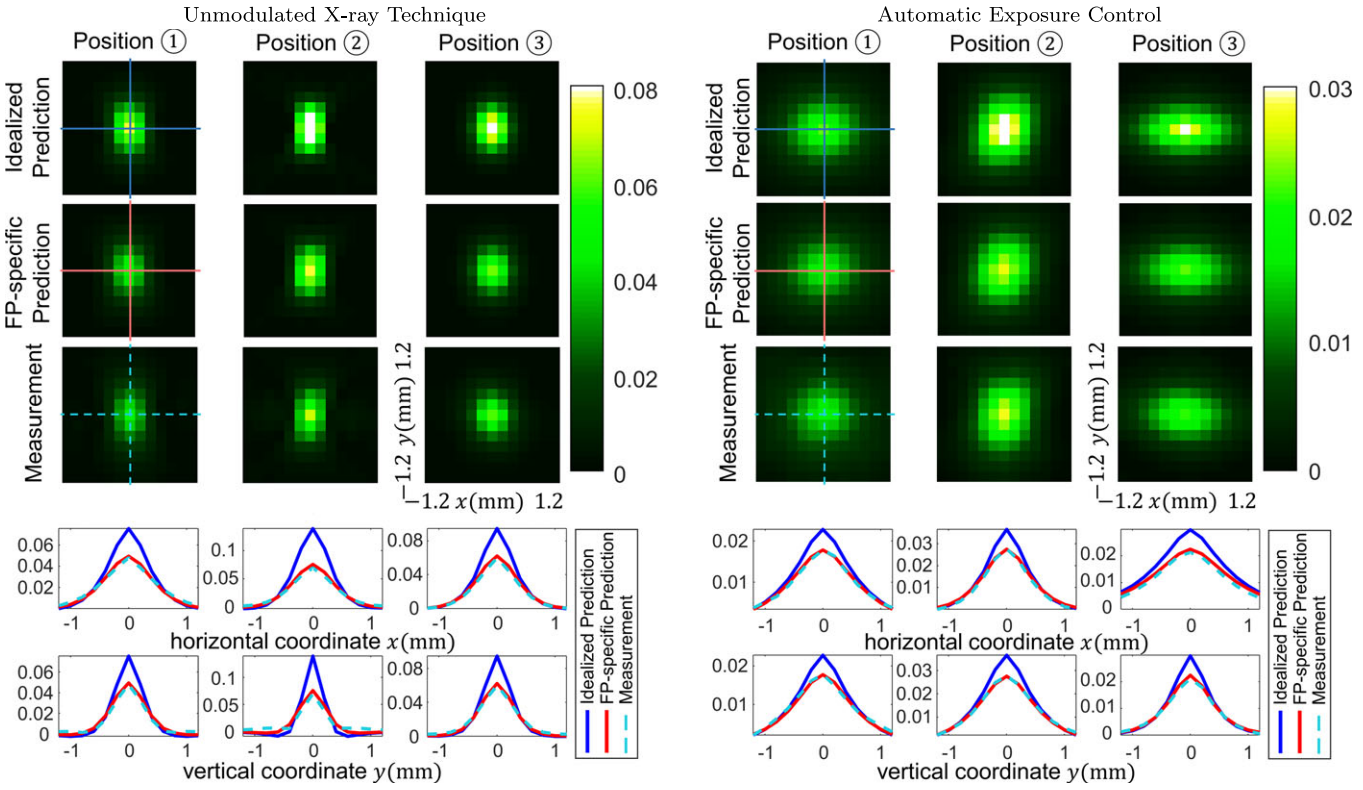

FIG. 6. PSF predictions and measurements for unmodulated and AEC x-ray techniques. [Color figure can be viewed at wileyonlinelibrary.com]

second position (see profile plots for the unmodulated case), furthest from the rotation axis. We conjecture that this mismatch originated from approximated source blur at the center. A shift-variant source blur model should help reduce the mismatch.

Comparing AEC to unmodulated results, an increase in blur is observed. This is consistent with using the same regularization parameter β in both experiments. Recall that the average dose in the AEC scan was a quarter of that in unmodulated scan. Since smoothness is controlled by the relative importance of data fidelity and regularization terms, using the same regularization parameter but decreasing the data fidelity (via reduced fluence) results in more blur (as observed).

Under the conditions of uniform regularization and uniform x-ray illumination (e.g., no bowtie filter), varying levels of blur are also observed with regard to directional dependence. Specifically, since measurements associated with shorter path lengths will have higher data fidelity and thus less MBIR-induced blur along the direction of measurements. Thus, for the unmodulated case, we see increased blur in the vertical direction due to the decreased data fidelity (longer path lengths) for lateral projections over anterior–posterior or posterior–anterior projections. One also tends to see a preference for increased tangential blur toward the edge of objects since the data fidelity is high for the shorter paths. Thus, for the elliptical phantom and the unmodulated beam, the central position shows preferential vertical smoothing and increased vertical smoothing in lateral position 2. The two effects (preferential vertical blur due to the ellipse and tangential blur) counteract each other in position 3 to yield a more isotropic response. For the AEC case, the data acquisition is modified so that the fluence arriving at the detector is constant for the central ray on the detector. Thus, all projection rays passing through the central position 1 have equal data fidelity, which results in a nearly isotropic blur. For the other two positions, AEC partially compensates for the asymmetry of the ellipse, whereas the tangential blur remains. If one desires uniform isotropic resolution for all image locations (using uniform regularization),a more sophisticated spatial fluence-field modulation that can homogenize the noise (e.g., dynamic bowtie filters,[68] multiple aperture device,[69] etc.) for all detector rays is required.

Figure 7 shows the β-dependent full-width half-maximum (FWHM) of the PSF at position with varying regularization strength. Specifically, β was swept linearly in the exponent with a $10^{0.5}$ step size, from $10^{4.5}$ to $10^{6.5}$. Measurements are plotted in cyan with 98% confidence intervals estimated with eight samples at each point. The red line represents the FP-specific prediction results and the blue line stands for idealized prediction. When regularization strength β was increased, the PL reconstruction exhibits increased overall blur. The proposed flat-panel-specific predictor outperforms the idealized predictor which systematically underestimates the blur in the reconstruction. We note there is a small degree of mismatch for the flat-panel-specific predictor at the lower regularization levels. Similarly, the measured PSFs are slightly blurrier than flat-panel-specific predictions. We conjecture that this may result from slight errors in the geometric calibration procedure that are not integrated in the prediction model.

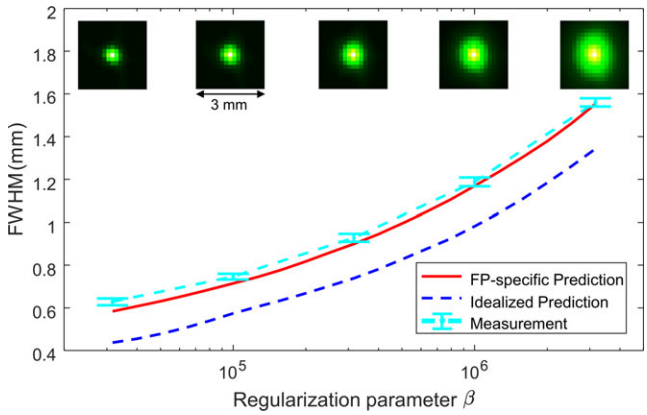

FIG. 7. Accuracy of predictions with varying regularization strength. Plots of PSF FWHM vs β are shown for idealized and flat-panel-specific predictors as well as measurements. Subfigures show the measured PSF at each β. [Color figure can be viewed at wileyonlinelibrary.com]

3.C. Local noise predictor validation

Figures 8 and 9 summarize the results of the noise predictor validation in specialized phantom study, showing the comparison between measurements and predictions in the unmodulated and AEC experiments, respectively. In each subfigure, NPS estimates are organized similar to the spatial resolution studies with each row showing an NPS computed by measurement or one of the two predictors. Each column represents one of the locations being compared. The measurements are somewhat noisy due to the limited number of ROIs used in the sliding window estimate. However, the general shape and amplitude are apparent and matched well with flat-panel-specific predictions. The idealized predictions underestimated noise level (variance) by over 70%. Comparing results across columns, we can see shift-variant noise properties at the three different positions. In each figure, the left subfigure shows NPS in reconstruction with regularization parameter $\beta = 10^4$, and the right shows results when $\beta = 10^5$. Consistent with expectations, higher regularization strength leads to reduced high frequency noise and smaller overall variance.

We also observe significant differences in noise properties between two acquisition strategies. Increased correlated noise is observed along f_y-axis in the unmodulated reconstructions because of fewer photons transmitted parallel to the long axis (x-axis in spatial domain) of the elliptical phantom. The overall noise distribution is more uniform and isotropic in AEC scans due to the increased homogeneity of the statistical weights.

3.D. Validation in anthropomorphic phantom studies

The results of spatial resolution and noise properties predictions and measurements in anthropomorphic phantom studies are summarized in Fig. 10 . The PSF at each location is shown in columns on the left and the NPS estimates are shown on the right. From the top to the bottom, each row shows the idealized predictions, flat-panel-specific predictions, and estimates in physical measurements. Central

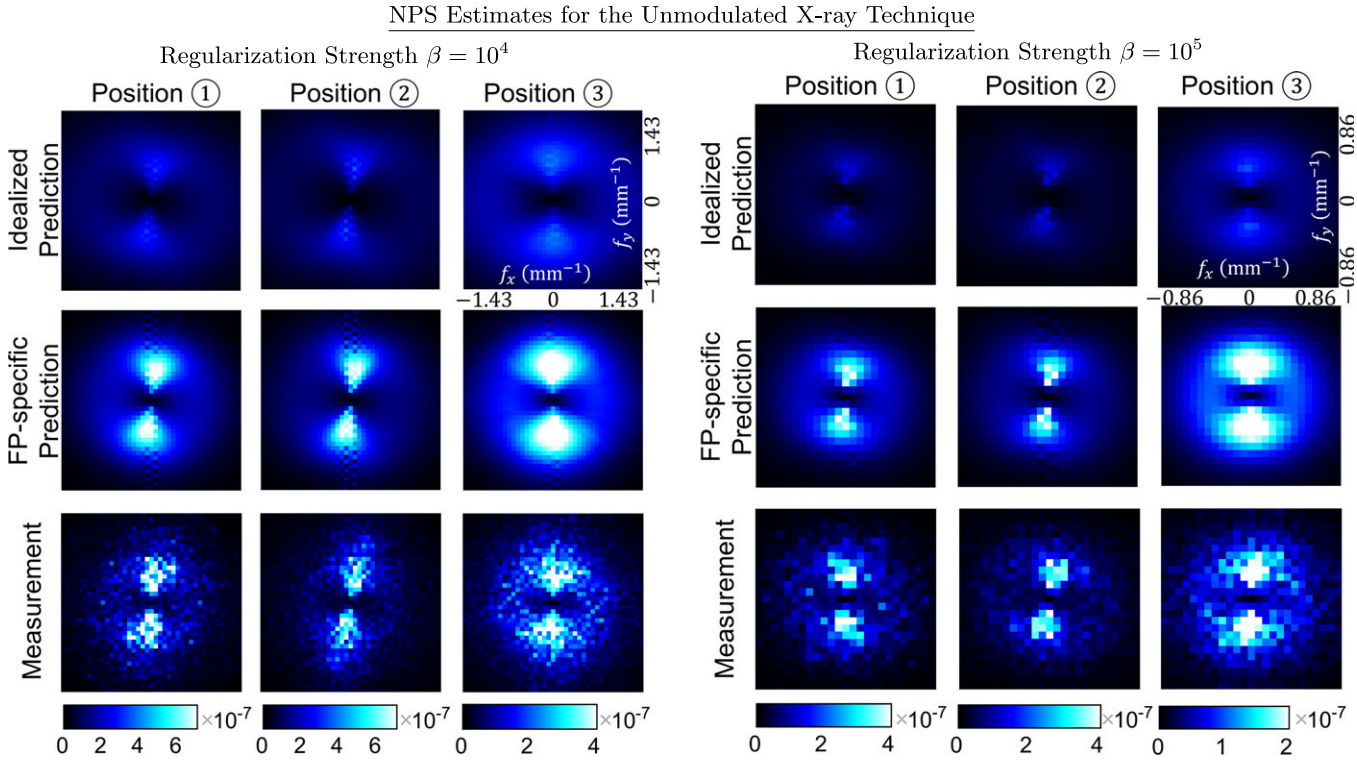

FIG. 8. Predicted and measured NPS estimates for the unmodulated x-ray technique. Left: $\beta = 10^4$; right: $\beta = 10^5$. Note that the colormaps vary for each column for better visualization due to location-dependent noise levels. [Color figure can be viewed at wileyonlinelibrary.com]

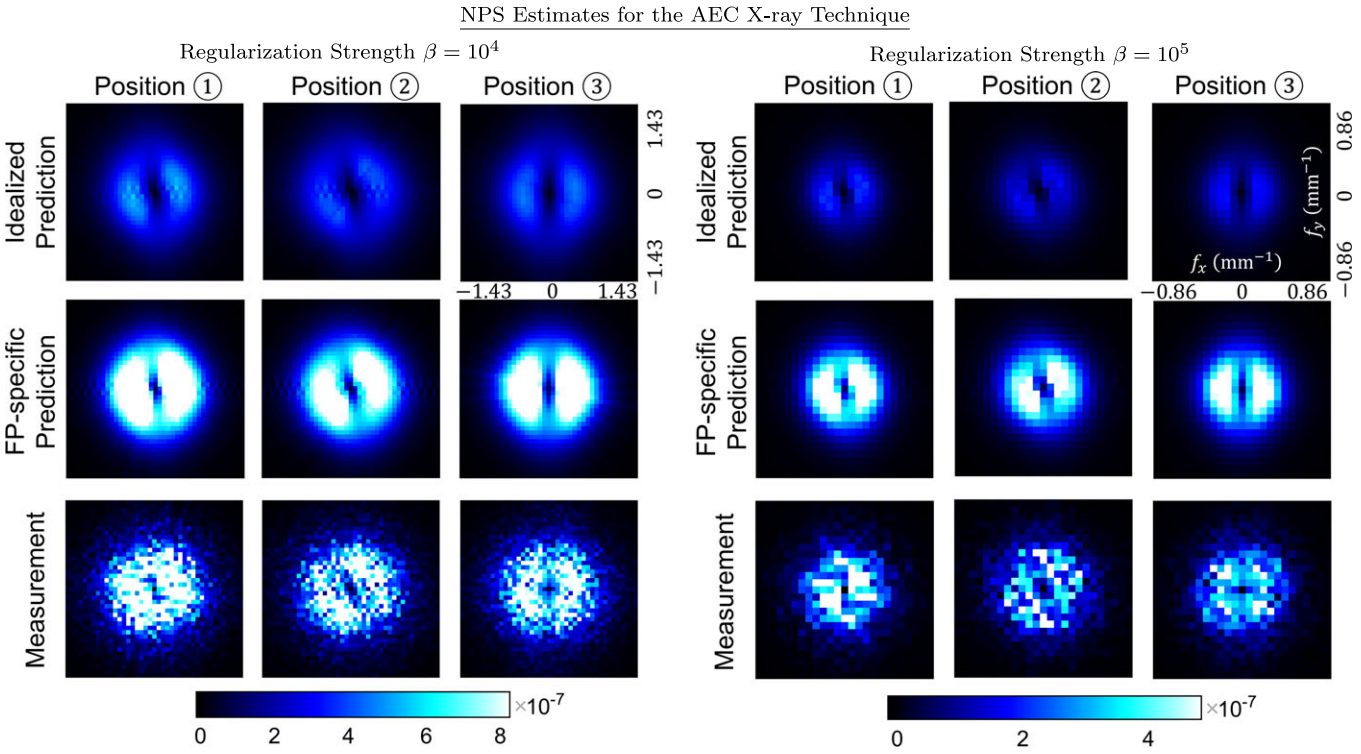

FIG. 9. Predicted and measured NPS estimates using the AEC x-ray technique. Left: $\beta = 10^4$; right: $\beta = 10^5$. For each regularization strength, the colormap is the same for every subfigure. [Color figure can be viewed at wileyonlinelibrary.com]

profiles in both horizontal and vertical directions of predictions and measurements are compared in the plots at the left bottom rows. The PL regularization parameter was $\beta = 10^6$ in the spatial resolution study, and $\beta = 10^5$ in the noise properties study.

In both spatial resolution and noise properties validations, the flat-panel-specific predictions closely match with the physical measurements, while the idealized PSF predictions are sharper (failing to capture the blur in the imaging system). Directional blurring due to the oblate phantom shape and shift variance of the response is evident with increased tangential blur for position 2 since it is closer to the edge of the phantom. The idealized NPS predictions underestimate the noise level in both locations; however, the proposed method shows good agreement with empirical NPS measurements. Nonstationarity of the noise is evident with very different NPS predictions between these two locations.

4. DISCUSSION AND CONCLUSION

In this work, we presented local spatial resolution and noise predictors for PL reconstruction that adopt realistic physical models of FP-CBCT data acquisition. Phantom experiments showed that FP-specific predictors have superior consistency to physical measurements when compared to idealized predictors of both spatial resolution and noise properties.

The proposed predictors account for the dependencies on patient anatomy, x-ray techniques, scanner geometry, and reconstruction penalty design through the weights, system matrix, and the Hessian matrix of quadratic penalty term. Moreover, they account for the dependency on system characteristics. The system characteristics including the scintillator blur, focal spot blur, aperture effect, and measurement covariance are precalibrated through direct x-ray measurements and used in properties prediction process. In our experiments, a one-time system characterization of the input–output relationship of the signal per unit incident x-ray is sufficient to provide an accurate set of predictors for both spatial resolution and noise properties. The accuracy of properties prediction is dependent on the precalibration and the stability of the system. We expect that detector effects like scintillator blur to be highly stable over time; however, there is the potential for additional complexity with focal spot blur. In particular, dependencies of focal spot size on tube current, tube heating, etc., have the potential to change the amount of blur induced by the source. To maintain accurate PSF and NPS predictions, such effects would need to be modeled to maintain high accuracy, for example, through calibration of focal spot blur as a function of tube current. While such effects were not significant in our experiments, different x-ray tubes and system geometries may be more susceptible to such effects.

These predictors can be used for prospective analysis of reconstructed image quality at any location of interest given measured projection data — permitting prospective control and design of regularization for specific image quality goals. Moreover, the same predictors can be used with different patient and object models for adaptive imaging whereby the acquisition approach (e.g., x-ray modulation) is adapted based on the patient anatomy. Similarly, since the proposed

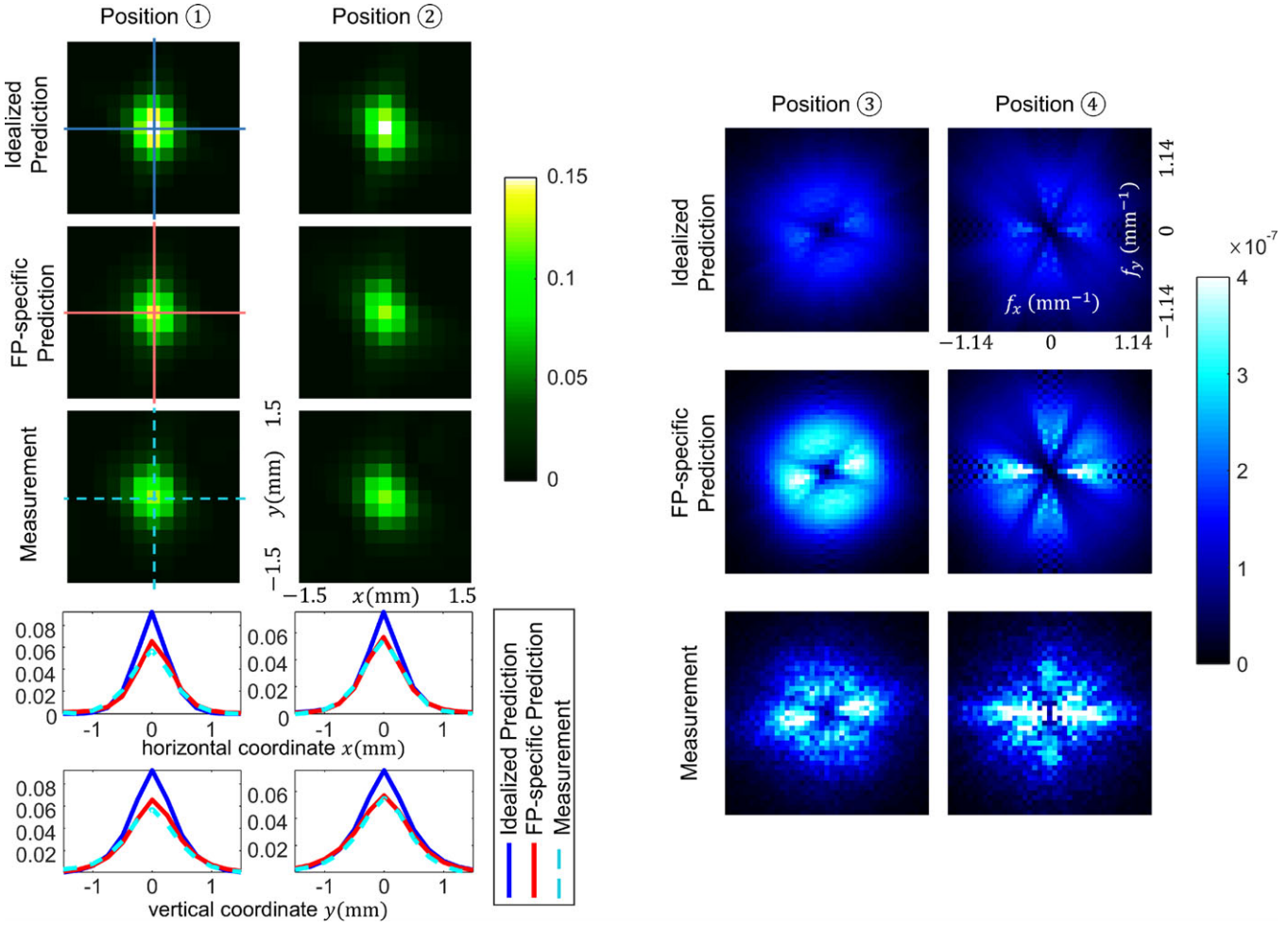

FIG. 10. PSF and NPS predictions and measurements in anthropomorphic phantom studies. [Color figure can be viewed at wileyonlinelibrary.com]

predictors take into account additional aspects of noise and resolution in an end-to-end system model (e.g., detector characterizations), these models may be used for joint design of hardware (including detector choices and system geometry) with MBIR software (which is known to improve image quality trade-offs over conventional analytics reconstruction approaches). As in related work, these improved local quantification of spatial resolution and noise properties can be further integrated into observer models, which are promising in prospective design of task-based optimization in system design, acquisition strategies, and reconstruction methods.

In this work, we adopted a FP-CBCT data acquisition forward model including the scintillator blur, an approximated shift-invariant focal spot blur, and the aperture effect. In FP-CBCT noise model, the general gain term associated with the Poisson-equivalent fluence level, I_0, in the reconstruction forward model is characterized along with the correlated noise level. However, these models leave out the shift-variant focal spot blur and the noise aliasing effect. The shift-variant property of focal spot blur is significant when large magnification is used. In such scenarios, more sophisticated modeling and system calibration are needed. Aliasing noise effects are small for indirect detection FP detectors due to the extra scintillator blur and is negligible in this work. In systems equipped with direct detection detector, noise remains high near and above the Nyquist frequency, and aliasing plays an important role. Thus, to accommodate such scenarios, this work needs to be extended to explicitly model aliasing.

In this work, we presented a general approach to assess PL-reconstructed image quality in a prospective fashion, especially in systems where characteristics such as system blur and nonideal statistics lead to the mismatch between the data acquisition model and the reconstruction model. This mismatch is significant in FP-CBCT systems since scintillator blur is nonnegligible. In conventional CT, mechanisms like a pixelated scintillator are utilized to avoid signal sharing between pixels. However, effects like charge sharing between adjacent pixels[70] and finite focal spot[71] can produce additional system blur that is often not modeled in reconstruction. Such blur may be potential impact in the prediction of imaging properties in high resolution CT applications. The proposed predictors are sufficiently general to accommodate such high resolution CT applications but will require system-specific calibration. While this work focused closely on PL with a quadratic penalty in CBCT, there is ongoing work to apply similar predictors and analysis of other reconstruction

method and regularization strategies (including edge-preserving penalties[41] and prior image-based reconstruction methods[72]). The methodology presented here is general — permitting mismatch between the data acquisition model and the reconstruction model (which often makes idealizations to obtain practical algorithms). To accommodate other reconstruction techniques, one may derive the properties predictors based on the corresponding acquisition and reconstruction model. For example, penalized weighted least squares (PWLS) is commonly used for reconstruction presuming a Gaussian statistical model for the line integral estimates, and it is straightforward to derive similar resolution and noise predictors for PWLS. In fact, since the derivations rely only on the first- and second-order statistics, the predictors for PWLS should be very similar to the Poisson PL case developed here if a conventional weighting scheme (the inverse of measurements) is applied.

In general, this work represents a bridge between the high-fidelity physical modeling common in detector and system design with cascaded systems analysis and model-based reconstruction, providing prospective image quality analysis of a CT system end-to-end and facilitating precise characterization and control of image properties without specialized data acquisitions and exhaustive reconstruction.

ACKNOWLEDGMENTS

This research was supported by the National Institutes of Health Grants U01-EB-018758 and a Johns Hopkins University Catalyst Grant.

APPENDIX (A1)

A RELATIONSHIP BETWEEN GAIN FACTORS IN FLAT-PANEL AND RECONSTRUCTION MODELS

Raw projection data acquired in FP-CBCT requires preprocessing including models/corrections for detector sensitivity, incident fluence inhomogeneities, and dark current. To eliminate these effects, a gain-offset preprocessing pipeline is typically used to normalize the projection data to the ratio of detected fluence and incident fluence, which should equal the exponent of the negative line integral according to a simple Beer–Lambert's law model. That is,

$$y_{\text{corr}} = \frac{y - \bar{y}_{\text{off}}}{\bar{y}_0 - \bar{y}_{\text{off}}}, \bar{y}_{\text{corr}} = \exp(-\mathbf{A}\mu) \tag{A1}$$

where y is one frame of uncorrected projection data, $\bar{y}_0$ is an estimated gain based on the average of bare-beam frames, and $\bar{y}_{\text{off}}$ is an offset estimated based on the average of dark frame with no x-ray exposure.

To perform model-based reconstruction, one must estimate I_0 in Eq. (13). This term carries important information about incident fluence levels and noise levels. Under a Poisson noise model assumption, I_0 can be calculated so that the scaled projection in bare-beam data $I_0 y_{0,\text{corr}}$ has equal mean and variance. Thus,

$$I_0 \bar{y}_{0,\text{corr}} = I_0^2 \sigma^2_{y_{0,\text{corr}}} \tag{A2}$$

$$I_0 = \frac{\bar{y}_{0,\text{corr}}}{\sigma^2_{y_{0,\text{corr}}}} = \frac{(\bar{y}_0 - \bar{y}_{\text{d}})^2}{\sigma^2_{y_0}}. \tag{A3}$$

Using cascaded system analysis, the local mean and variance of the same bare-beam data including detector response are

$$\bar{y}_0 = k^{-1} a_{\text{pd}}^2 \bar{q}_0 \bar{g}_1 \bar{g}_2 \bar{g}_4 + \bar{y}_{\text{d}} = a_{\text{pd}}^{-2} \bar{q}_0 G_0 + \bar{y}_{\text{d}} \tag{A4}$$

$$\sigma^2_{y_0} = k^{-2} \int\int S_{\text{det}} df_{\text{u}} df_{\text{v}} \tag{A5}$$

$$= k^{-2} a_{\text{pd}}^4 \bar{q}_0 \bar{g}_1 \bar{g}_2 \bar{g}_4 \int\int (1 + \bar{g}_4 P_K T_3^2) T_{\text{a}}^2 df_{\text{u}} df_{\text{v}} + \sigma^2_{\text{ro}} \tag{A6}$$

$$= k^{-2} \bar{q}_0 G_0 \int\int (1 + \gamma_c T_{\text{sc}}^2) T_{\text{a}}^2 df_{\text{u}} df_{\text{v}} + \sigma^2_{\text{ro}} \tag{A7}$$

where k is the conversion gain that denotes the number of electrons per arbitrary detector unit. The remaining notation is consistent with Section 2.A.2. Combining Eqs. (A3), (A4), and (A7), the analytical expression for the I_0 estimate is

$$I_0 = \frac{a_{\text{pd}}^{-4} q_0^2 G_0^2}{\bar{q}_0 G_0 \int\int (1 + \gamma_c T_{\text{sc}}^2) T_{\text{a}}^2 df_{\text{u}} df_{\text{v}} + \sigma^2_{\text{ro}}}. \tag{A8}$$

Presuming that the readout noise is relatively small compared to the quantum noise permits the following approximation:

$$I_0 = \frac{a_{\text{pd}}^{-4} q_0 G_0}{\int\int (1 + \gamma_c T_{\text{sc}}^2) T_{\text{a}}^2 df_{\text{u}} df_{\text{v}}}. \tag{A9}$$

In Eq. (28), we introduce an empirical gain G that scales the corrected data $I_0 y_{\text{corr}}$ to the detector output,

$$G I_0 y_{\text{corr}} = \bar{q}_0 G_0 y_{\text{corr}} \tag{A10}$$

where the incident quanta $\bar{q}_0$ is attenuated by the object to $\bar{q}_0 y_{\text{corr}}$. Thus, the explicit expression of G can be written as,

$$G = a_{\text{pd}}^4 \int\int (1 + \gamma_c T_{\text{sc}}^2) T_{\text{a}}^2 df_{\text{u}} df_{\text{v}}. \tag{A11}$$

This is the scalar gain factor used in Section 2.B.2.

[a)]Author to whom correspondence should be addressed. Electronic mail: web.stayman@jhu.edu.

REFERENCES

1. Clark DP, Badea CT. Micro-CT of rodents: state-of-the-art and future perspectives. *Phys Med*. 2014;30:619–634.

2. Chen B, Ning R. Cone-beam volume CT breast imaging: feasibility study. *Med Phys*. 2002;29:755–770.
3. Wu T, Stewart A, Stanton M, et al. Tomographic mammography using a limited number of low-dose cone-beam projection images. *Med Phys*. 2003;30:365–380.
4. Scarfe WC, Farman AG, Sukovic P. Clinical applications of cone-beam computed tomography in dental practice. *J Can Dent Assoc*. 2006;72:75–80.
5. Patel S, Dawood A, Pitt Ford T, Whaites E. The potential applications of cone beam computed tomography in the management of endodontic problems. *Int Endod J*. 2007;40:818–830.
6. Veldhoen S, Schöllchen M, Hanken H, et al. Performance of cone-beam computed tomography and multidetector computed tomography in diagnostic imaging of the midface: a comparative study on Phantom and cadaver head scans. *Eur Radiol*. 2017;27:790–800.
7. Jaffray DA, Siewerdsen JH, Wong JW, Martinez AA. Flat-panel cone-beam computed tomography for image-guided radiation therapy. *Int J Radiat Oncol Biol Phys*. 2002;53:1337–1349.
8. Siewerdsen JH, Moseley DJ, Burch S, et al. Volume CT with a flat-panel detector on a mobile, isocentric C-arm: pre-clinical investigation in guidance of minimally invasive surgery. *Med Phys*. 2005;32:241–254.
9. Orth RC, Wallace MJ, Kuo MD. C-arm Cone-beam CT: general principles and technical considerations for use in interventional radiology. *J Vasc Interv Radiol*. 2008;19:814–820.
10. Morimoto M, Numata K, Kondo M, et al. C-Arm Cone Beam CT for hepatic tumor ablation under real-time 3D imaging. *Am J Roentgenol*. 2010;194:W452–W454.
11. Bapst B, Lagadec M, Breguet R, Vilgrain V, Ronot M. Cone beam computed tomography (CBCT) in the field of interventional oncology of the liver. *Cardiovasc Intervent Radiol*. 2016;39:8–20.
12. Siewerdsen JH, Zbijewski W, Xu J. Cone beam CT image quality. *Cone Beam Comput Tomogr*. 2014;4:37–58.
13. ICRU. ICRU REPORT 41-Modulation Transfer Function of Screen-film Systems. tech. rep. 1986.
14. Siewerdsen JH. Signal, noise, and detective quantum efficiency of a-Si: H flat-panel imagers. 1998.
15. Zhao C, Kanicki J, Konstantinidis AC, Patel T. Large area CMOS active pixel sensor x-ray imager for digital breast tomosynthesis: analysis, modeling, and characterization. *Med Phys*. 2015;42:6294–6308.
16. Tward DJ, Siewerdsen JH. Cascaded systems analysis of the 3D noise transfer characteristics of flat-panel cone-beam CT. *Med Phys*. 2008;35:5510–5529.
17. Gang GJ, Tward DJ, Lee J, Siewerdsen JH. Anatomical background and generalized detectability in tomosynthesis and cone-beam CT. *Med Phys*. 2010;37:1948–1965.
18. Pineda AR, Tward DJ, Gonzalez A, Siewerdsen JH. Beyond noise power in 3D computed tomography: The local NPS and off-diagonal elements of the Fourier domain covariance matrix. *Med Phys*. 2012;39:3240–3252.
19. Gang GJ, Zbijewski W, Stayman JW, Siewerdsen JH, Gang GJ. Cascaded systems analysis of noise and detectability in dual-energy cone-beam CT Cascaded systems analysis of noise and detectability in dual-energy conebeam CT. *Med Phys*. 2012;39:5145–5156.
20. Xu J, Sisniega A, Zbijewski W, et al. Modeling and design of a cone-beam CT head scanner using task-based imaging performance optimization. *Phys Med Biol*. 2016;61:3180-3207.
21. Cao Q, Sisniega A, Brehler M, et al. Modeling and evaluation of a high-resolution CMOS detector for conebeam CT of the extremities. *Med Phys*. 2017;45:114–130.
22. Barrett HH, Furenlid LR, Freed M, et al. Adaptive SPECT. *IEEE Trans Med Imaging*. 2008;27:775–788.
23. Gang GJ, Siewerdsen JH, Stayman JW. Joint optimization of fluence field modulation and regularization in task-driven computed tomography. *Proc SPIE*. 2017;10132:101320E–101320E-7.
24. Beister M, Kolditz D, Kalender WA. Iterative reconstruction methods in X-ray CT. *Phys Med*. 2012;28:94–108.
25. Prakash P, Kalra MK, Digumarthy SR, et al. Radiation dose reduction with chest computed tomography using adaptive statistical iterative reconstruction technique: initial experience. *J Comput Assist Tomogr*. 2010;34:40-45.
26. Chang W, Lee JM, Lee K, et al. Assessment of a model-based, iterative reconstruction algorithm (MBIR) regarding image quality and dose reduction in liver computed tomography. *Invest Radiol*. 2013;48:598–606.
27. Zhang R, Thibault JB, Bouman CA, Sauer KD, Hsieh J. Model-based iterative reconstruction for dual-energy X-ray CT using a joint quadratic likelihood model. *IEEE Trans Med Imaging*. 2013;33:1–18.
28. Nuyts J, De Man B, Fessler JA, Zbijewski W, Beekman FJ. Modelling the physics in the iterative reconstruction for transmission computed tomography. *Phys Med Biol*. 2013;58:R63.
29. Willemink MJ, De Jong PA, Leiner T, et al. Iterative reconstruction techniques for computed tomography Part 1: technical principles. *Eur Radiol*. 2013;23:1623-1631.
30. Wang G, Zhou J, Yu Z, Wang W, Qi J. Hybrid pre-log and post-log image reconstruction for computed tomography. *IEEE Trans Med Imaging*. 2017;36:2457–2465.
31. Enjilela E, Lee TY, Hsieh J, et al. Ultra-low dose quantitative CT myocardial perfusion imaging with sparse- view dynamic acquisition and image reconstruction: a feasibility study. *Int J Cardiol*. 2017;254:272–281.
32. Gang GJ, Stayman JW, Zbijewski W, Siewerdsen JH. Task-based detectability in CT image reconstruction by filtered backprojection and penalized likelihood estimation. *Med Phys*. 2014;41:081902.
33. Richard S, Husarik DB, Yadava G, Murphy SN, Samei E. Towards task-based assessment of CT performance: system and object MTF across different reconstruction algorithms. *Med Phys*. 2012;39:4115–4122.
34. Yu L, Vrieze TJ, Leng S, et al. Technical Note: measuring contrast- and noise-dependent spatial resolution of an iterative reconstruction method in CT using ensemble averaging. *Med Phys*. 2015;42:2261–2267.
35. Li K, Tang J, Chen GH. Statistical model based iterative reconstruction (MBIR) in clinical CT systems: experimental assessment of noise performance. *Med Phys*. 2014;41:041906.
36. Solomon J, Samei E. Quantum noise properties of CT images with anatomical textured backgrounds across reconstruction algorithms: FBP and SAFIRE. *Med Phys*. 2014;41:091908.
37. Fessler JA, Rogers WL. Spatial resolution properties of penalized-likelihood image reconstruction: space- invariant tomographs. *IEEE Trans Image Process*. 1996;5:1346-1358.
38. Qi J, Leahy RM. Resolution and noise properties of MAP reconstruction for fully 3-D PET. *IEEE Trans Med Imaging*. 2000;19:493-506.
39. Fessler JA. Mean and variance of implicitly defined biased estimators (Such as penalized maximum likelihood): applications to tomography. *IEEE Trans Image Process*. 1996;5:493-506.
40. Zhang-O'Connor Y, Fessler JA. Fast predictions of variance images for fan-beam transmission tomography with quadratic regularization. *IEEE Trans Med Imaging*. 2007;26:335-346.
41. Schmitt S, Goodsitt M, Fessler J. Fast variance prediction for iteratively reconstructed CT images with locally quadratic regularization. *IEEE Trans Med Imaging*. 2016;PP:17–26.
42. Stayman JW, Fessler JA. Regularization for uniform spatial resolution properties in penalized-likelihood image reconstruction. *IEEE Trans Med Imaging*. 2000;19:601–615.
43. Stayman JW, Fessler JA. Compensation for nonuniform resolution using penalized-likelihood reconstruction in space-variant imaging systems. *IEEE Trans Med Imaging*. 2004;23:269-284.
44. Cho JH, Fessler JA. Regularization designs for uniform spatial resolution and noise properties in statistical image reconstruction for 3-D X-ray CT. *IEEE Trans Med Imaging*. 2015;34:678–689.
45. Dang H, Stayman J, Xu J, Task-based regularization design for detection of intracranial hemorrhage in conebeam CT. *Fourth Int Conf Image Form X-ray Comput Tomogr*. 2016:557–560.
46. Stayman JW, Siewerdsen JH. Task-based trajectories in iterative reconstructed interventional cone-beam CT. *Int Meet Fully Three-Dimensional Image Reconstr Radiol Nucl Med*. 2013:257–260.
47. Fischer A, Lasser T, Schrapp M, Stephan J, Noël PB. Object specific trajectory optimization for industrial x-ray computed tomography. *Sci Rep*. 2016;6:1–9.
48. Gang GJ, Siewerdsen J, Stayman J. Taskdriven optimization of CT tube current modulation and regularization in model-based iterative reconstruction. *Phys Med Biol*. 2017;62:4777–4797.
49. Fessler JA. Spatial Resolution properties of penalized weighted least-squares tomographic image reconstruction with model mismatch. tech. rep.University of Michigan, Ann Arbor 1997.

50. Zheng J, Fessler JA, Chan HP. Detector blur and correlated noise modeling for digital breast tomosynthesis reconstruction. *IEEE Trans Med Imaging*. 2018;37:116–127.
51. Tilley II S, Siewerdsen JH, Stayman JW. Model-based iterative reconstruction for flat-panel cone-beam CT with focal spot blur, detector blur, and correlated noise. *Phys Med Biol*. 2016;61:296–319.
52. Wang W, Gang GJ, Stayman JW. Spatial resolution properties in penalized-likelihood reconstruction of blurred tomographic data. *Proc Int Meeting Fully Three-Dimensional Image Reconstr Radiol Nucl Med*. 2017;14:702–707.
53. Wang W, Gang GJ, Siewerdsen JH, Stayman JW. Spatial resolution and noise prediction in flatpanel cone-beam CT penalized-likelihood reconstruction. *Proc SPIE Int Soc Opt Eng*. 2018; 10573:1057346.
54. Tilley II S, Jacobson M, Cao Q, et al. Penalized likelihood reconstruction with high-fidelity measurement models for high-resolution cone-beam imaging. *IEEE Trans Med Imaging*. 2017:37:988–999.
55. Tilley II S, Zbijewski W, Siewerdsen JH, Stayman JW. Modeling shift-variant X-ray focal spot blur for high resolution flat-panel cone-beam CT. *Conf Proc Int Conf Image Form Xray Comput Tomogr*. 2016;2016:463–466.
56. Long Y, Fessler JA, Balter JM. 3D forward and back-projection for X-ray CT using separable footprints. *IEEE Trans Med Imaging*. 2010;29:1839–1850.
57. Rabbani M, Shaw R, Van Metter R. Detective quantum efficiency of imaging systems with amplifying and scattering mechanisms. *J Opt Soc Am A Opt Image Sci*. 1987;4:895–901.
58. Siewerdsen JH, Antonuk LE, El-Mohri Y, Yorkston J, Huang W, Cunningham IA. Signal, noise power spectrum, and detective quantum efficiency of indirect-detection flat-panel imagers for diagnostic radiology. *Med Phys*. 1998;25:614628.
59. Zhao W, Ji WG, Debrie A, Rowlands JA. Imaging performance of amorphous selenium based flat-panel detectors for digital mammography: Characterization of a small area prototype detector. *Med Phys*. 2003;30:254-263.
60. Siewerdsen JH, Antonuk LE, El-Mohri Y, et al. Empirical and theoretical investigation of the noise performance of indirect detection, active matrix flat-panel imagers (AMFPIs) for diagnostic radiology. *Med Phys*. 1997;24:71–89.
61. Richard S, Siewerdsen JH, Jaffray DA, Moseley DJ, Bakhtiar B. Generalized DQE analysis of radiographic and dual-energy imaging using flat-panel detectors. *Med Phys*. 2005;32:1397–1413.
62. Samei E, Flynn MJ, Reimann DA. A method for measuring the presampled MTF of digital radiographic systems using an edge test device. *Med Phys*. 1998;25:102-113.
63. Gies M, Kalender WA, Wolf H, Suess C, Madsen MT. Dose reduction in CT by anatomically adapted tube current modulation. I. Simulation studies. *Med Phys*. 1999;26:2248–2253.
64. Fessler JA, Erdogan H. A paraboloidal surrogates algorithm for convergent penalized-likelihood emission image reconstruction. 1998 IEEE Nuclear Science Symposium Conference Record 1998 IEEE Nuclear Science Symposium and Medical Imaging Conference Cat No98CH36255. 1998;2:1132–1135.
65. Erdogan H, Fessler JA. Monotonic algorithms for transmission tomography. *IEEE Trans Med Imaging*. 1999;18:801–814.
66. Erdogan H, Fessler JA. Ordered subsets algorithms for transmission tomography. *Phys Med Biol*. 1999;44:2835–2851.
67. Jaffray AD, Siewerdsen JH. Cone-beam computed tomography with a flat-panel imager: initial performance characterization. *Med Phys*. 2000;27:1311–1323.
68. Mao A, Shyr W, Gang GJ, Stayman JW. Dynamic beam filtering for miscentered patients. *SPIE Med Imaging*. 2018;10573:105730U.
69. Wang W, Gang GJ, Mao A, Sisniega A, Siewerdsen JH, Stayman JW. Volume-of-interest CT imaging with dynamic beam filtering using multiple aperture devices. in *Conf Proc Int Conf Image Form Xray Comput Tomogr* 2018;2018:213–217.
70. Hsieh J. *Computed Tomography: Principles, Design, Artifacts and Recent Advances*. 2nd ed. Bellingham, WA: SPIE; 2009.
71. Fu L, Wang J, Rui X, Thibault JB, De Man B. Modeling and estimation of detector response and focal spot profile for high-resolution iterative CT reconstruction. *IEEE Nucl Sci Symp Conf Rec*. 2013;2013:1–5.
72. Zhang H, Gang GJ, Dang H, Stayman JW. Regularization analysis and design for prior-image-based X-ray CT reconstruction. *IEEE Trans Med Imaging*. 2018;14:1–1.